Chemical Physics 138 (1989) 89–98
North-Holland, Amsterdam

THE LOW-LYING ELECTRONIC STATES OF INDIUM TRIMER

Ping Yi FENG and K. BALASUBRAMANIAN [1]
Department of Chemistry, Arizona State University, Tempe, AZ 85287–1604, USA

Received 17 March 1989

Multi-configuration SCF (MCSCF) followed by multi-reference singles+doubles CI (MRSDCI) calculations which included up to 177000 configurations are carried out on seven low-lying electronic states of indium trimer ($^4A_2$, $^4B_1$, $^2B_1$, $^4B_2$, $^2A_1$, $^2B_2$ and $^4A_1$). Two nearly degenerate electronic states of $^4A_2$ and $^4B_1$ symmetries with isosceles triangular geometries are found as the candidates for the ground state. The spin–orbit effects are included through a relativistic configuration interaction method (RCI). The electronic states of In_3 are compared with Ga_3. The bending potential energy surfaces of seven electronic states of In_3 are also obtained. The nature of bondings and potential energy surfaces are analyzed.

1. Introduction

The electronic structural properties of small metal and semi-conductor clusters have been the topics of many investigations in recent years [1–25]. The spectroscopic investigations of small metal clusters have been on the increase due to the advent of supersonic nozzle expansion method, matrix-isolation of clusters and negative ion photodetachment spectroscopic methods. These clusters have a large number of electronic states with varied spatial and spin symmetries and geometries. Thus, their electronic spectra tend to be complex. Theoretical investigations of heavy clusters are quite challenging due to the problem of electron correlation, large relativistic corrections and the existence of very densely packed electronic states for such clusters.

The clusters of GaAs of composition Ga_xAs_y, InSb of composition In_xSb_y as well as $In_xP_y^-$ have been generated in recent years using laser vaporization methods [5,17]. Both the Ga_xAs_y, In_xSb_y and $In_xP_y^-$ clusters exhibit interesting even–odd alternations and photofragmentation patterns. Duncan and co-workers [18–21] have also examined the photofragmentation patterns of other main group clusters such as Sb_x and Bi_x.

There are no theoretical calculations to date on indium trimer, although in our laboratory the spectroscopic constants and potential energy curves of electronic states of the indium dimer have been obtained [24]. There exists some controversy in the literature on the nature of isoelectronic Al_3 cluster. The experimental ESR spectra in the rare gas matrix favor a quartet ground state for Al_3 while a recent MCSCF calculation by Basch [15] predicts the ground state to be of $^2A_1$ symmetry. Jet-cooled spectra of Al_3 have also been obtained recently [25]. In an earlier investigation, the present authors [12] have examined the electronic states of neutral Ga_3 and Ga_3^+. These calculations revealed existence of seven low-lying electronic states of Ga_3.

Relativistic and spin–orbit effects in addition to electron correlation effects are expected to be large for In_3. The general theory and trends of bonding in metallic clusters have been discussed by McAdon and Goddard [26] using generalized valence bond methods. In particular these authors have discussed bonding in Li_3, Li_3^-, Ag_3, etc. In this investigation, we carry out complete-active space MCSCF (CASSCF) followed by multireference singles+doubles CI (MRSDCI) calculations on seven electronic states of In_3. We also carry out relativistic CI (RCI) calculations using the MRSDCI natural orbitals to compute the spin–orbit effects. The electronic and structural properties of In_3 are compared with Ga_3. Section 2

[1] Camille and Henry Dreyfus Teacher-Scholar.

describes our method of calculations while section 3 comprises results and discussions.

2. Method of calculations

In an earlier investigation, we have outlined in detail the method of calculations for Ga_3 [12]. In the present investigation, we use a similar method except that both electron correlation effects and spin–orbit effects are taken into account to a higher degree. We oriented the In_3 cluster on the *yz* plane with the *z* axis bisecting the In–In–In apex angle of the isosceles triangle. Seven electronic states of different spatial and spin symmetries arising from the ^2P ground state of the indium atom are considered. All calculations reported here were carried out in the C_{2v} point group. The rationale for choosing seven electronic states is that there are eight possible doublet and quartet states in C_{2v} symmetry of which the $^2A_2$ state was found to be much higher for Ga_3.

Relativistic effective core potentials for the indium atom with the outer $5s^25p^1$ shell explicitly retained in the valence space are employed in the present calculations. The Gaussian analytical potentials together with the 3s3p Gaussian basis sets were taken from the work of LaJohn et al. [27]. We add to the (3s3p) set a single set of d polarization functions with the exponent 0.212. The error made in the omission of the d^{10} shell in the valence space should be less than 5% in geometries. In the present investigation, comparison calculations which included the $4d^{10}$ shells in the valence space also were carried out by employing another set of RECPs which included the $4d^{10}5s^25p^1$ in the valence space and the corresponding basis set. The errors in geometries were less than 2%.

MCSCF calculations were carried out to generate the orbitals for the configuration interaction (CI) calculations using the complete active space MCSCF method (CASSCF). In this method the most important electrons (active electrons) are distributed in all possible ways among a chosen set of the most important orbitals called the internal space of orbitals. The four outer 5s and 5p orbitals of each In atom in In_3 correlate into five a_1, four b_2, two b_1 and one a_2 orbitals in the C_{2v} group with the molecular orientation defined earlier. A CASSCF calculation which included all the 12 orbitals in the active space with nine electrons distributed in all possible ways generates too large a configuration space for our codes. As we [12] and Basch [15] suggested, the totally symmetric combination of the s orbitals on the metal atoms ($1a_1$ orbital) does not play a significant role in the CASSCF. Thus in our calculations, the $1a_1$ orbital was kept in core in the CASSCF in that excitations were not allowed from the $1a_1$ orbital. The fifth a_1 orbital was found to be quite antibonding and somewhat less important in the CASSCF. The seven remaining electrons were distributed in all possible ways among the remaining three a_1, three b_2, two b_1 and one a_2 orbitals in the CASSCF. Although no excitations were allowed from the $1a_1$ orbital in the CASSCF, CI calculations included excitations from this orbital.

Configuration interaction (CI) calculations were carried out following CASSCF. The CI calculations were carried out using the multireference singles+double CI (MRSDCI) method. In this method, all those configurations in the CASSCF with coefficients larger than or equal to 0.07 are included as reference configurations. Then single and double excitations were allowed from these reference configurations. Note that excitations from the $1a_1^2$ shell were also included in the MRSDCI. We also calculated the dipole moments and Mulliken populations of all the electronic states of In_3 from the natural orbitals of the MRSDCI calculations.

Spin–orbit effects were included following MRSDCI calculations using the recently developed relativistic CI (RCI) procedure for polyatomics [28]. In this method, low-lying electronic configurations of different spatial and spin symmetries which mix in the presence of the spin–orbit operator (same symmetry in the C_{2v}^2 double group) were included as reference configurations. Single and double excitations were allowed from these reference configurations. Spin–orbit integrals were obtained in the same Gaussian basis set using the differences of $l+1/2$ and $l-1/2$ relativistic ECPs as the spin–orbit operator. The RCI calculations of the $^2A_1\alpha$ state, for example, included $^2B_1\beta$, $^2B_2\beta$, $^2A_2\alpha$ states as reference configurations in addition to configurations of $^2A_1\alpha$ symmetry and other low-lying states of quartet symmetry. The RCI calculations without the spin–orbit operator were also carried out to find the effect of spin–orbit coupling.

The CASSCF calculations included between 940

and 1525 CSFs depending on the spin multiplicity of the electronic state. The MRSDCI calculations included up to 177000 configurations depending on the electronic state.

The CASSCF and MRSDCI calculations were carried our using one of the present authors' [29] modified version of the ALCHEMY II codes [#1]. The Mulliken population analysis was carried out using the modified ALCHEMY property package to exclude the $d_{x^2+y^2+z^2}$ population from the d and add it to the s. The spin–orbit integrals were calculated using Pitzer's modified version of ARGOS codes [30].

3. Results and discussions

3.1. Equilibrium geometries and potential energy surfaces

Table 1 shows the optimized bent equilibrium geometries and their energy separations at both CASSCF and MRSDCI levels of theory. Fig. 1 shows the optimized MRSDCI equilibrium geometries of the electronic states of In_3. Fig. 2 shows the actual bending potential energy surfaces for several electronic states obtained using the CASSCF method. As can be seen from table 1, the equilibrium geometries predicted by CASSCF calculations are not substantially different from the MRSDCI geometries. The bond lengths change at the most 0.13 Å. The bond angles change at the most 4° at the MRSDCI level of theory in comparison to the zeroth-order CASSCF level. Table 2 shows the equilibrium geometries and the energy separations of the linear electronic states of In_3.

Three nearly degenerate states of quartet symmetry ($^4A_2$, $^4B_1$, $^4\Sigma_u^-$) are possible candidates for the ground state. The MRSDCI calculations predict the $^4A_2$ state to be the lowest, although the $^4B_1$ state is only 0.01 eV above the $^4A_2$ state. The equilibrium geometries of both $^4A_2$ and $^4B_1$ states are isosceles triangles, although $^4B_1$ is very acute. Note that the linear limit of the $^4A_2$ ($^4\Sigma_u^-$) is also only 0.07 eV above the ground state.

The $^2B_1$ state exhibits a very acute geometry and thus the In–In bond lengths for the two-sides of the isosceles triangle are large. As can be seen from fig. 1, both $^4B_1$ and $^2B_1$ states have short In–In bond lengths at the base of the isosceles triangle. Thus, the $^4B_1$, $^2B_1$, and $^2A_1$ electronic states exhibit enhanced bonding at the base while the other states show greater bond strengths at the equal sides of the isosceles triangles.

The only electronic state with equilateral triangle geometry is the $^4B_2$ state. The $^4A_1$ electronic state has a linear geometry ($^4\Delta_g$).

Table 3 shows the effect including the $4d^{10}$ shells explicitly in the CASSCF calculations on geometries of the low-lying states of In_3. As can be seen from this table, the effect of the $4d^{10}$ shell on the bond lengths is less than 1.3% and on the bond angles is less than 0.5° for the three electronic states which we compared. Thus, the $4d^{10}$ core electrons do not play an important role in the determination of the geometries of the low-lying states of In_3.

[#1] The major authors of ALCHEMY II codes are B. Liu, B. Lengsfield and M. Yoshimine.

Table 1
Geometries and energies of the bent electronic states of In_3

CASSCF				MRSDCI			
state	θ (deg)	R [a] (Å)	E [b] (eV)	state	θ (deg)	R [a] (Å)	E [b] (eV)
$^4A_2$	75.2	2.97	0.0	$^4A_2$	71.04	2.95	0.0
$^4B_1$	54.8	3.25	0.03	$^4B_1$	55.2	3.12	0.01
$^2B_1$	47.6	3.37	0.07	$^2B_1$	48.9	3.31	0.11
$^2A_1$	49.6	3.60	0.28	$^4B_2$	60.0	3.29	0.35
$^4B_2$	58.4	3.39	0.35	$^2A_1$	51.0	3.49	0.45
$^2B_2$	74.3	3.17	0.37	$^2B_2$	74.4	3.04	0.45

[a] The two equal sides of the isosceles triangle; θ = apex angle.
[b] Zero energy for CASSCF is −5.513007 hartree; for MRSDCI is −5.609780 hartree; the zero energy is for the $^4A_2$ ground state at the reported geometry.

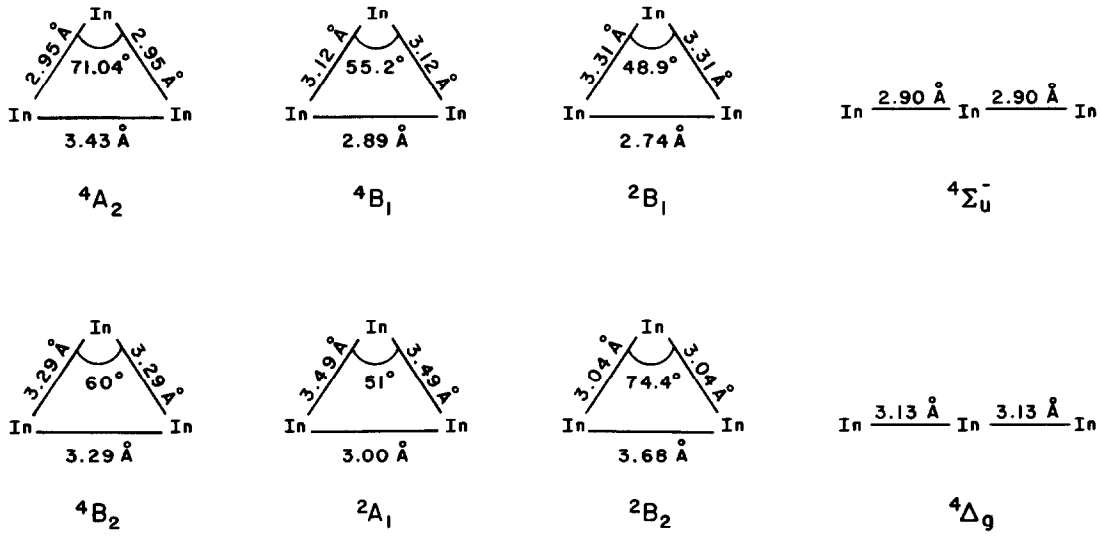

Fig. 1. The equilibrium MRSDCI geometries of eight electronic states of In_3. The $^2B_2$ and $^2A_1$ minima correspond to Jahn–Teller components of a $^2E'$ state (see section 3.2).

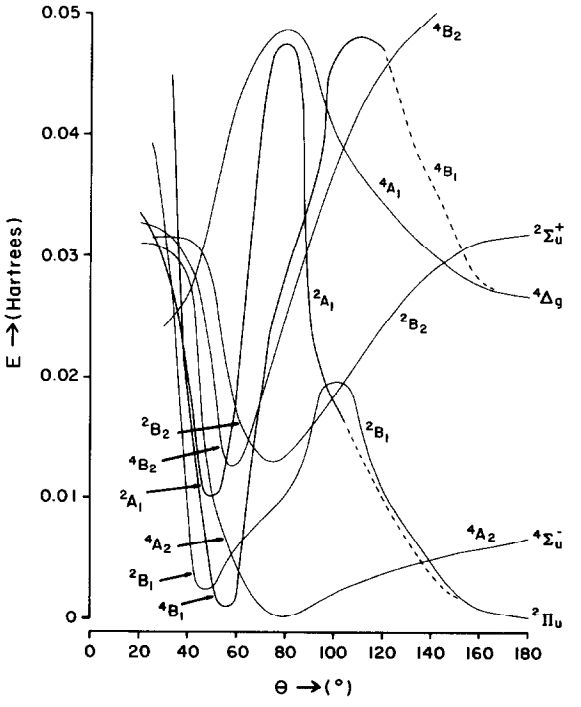

Fig. 2. The bending potential energy surfaces of low-lying states of In_3.

Table 2
Properties of the linear electronic states of In_3

CASSCF			MRSDCI		
state	R (Å)	E (eV)	state	R (Å)	E (eV)
$^2\Pi_u$	3.07	−0.02	$^4\Sigma_u^-$	2.90	0.07
$^4\Sigma_u^-$	2.90	0.18	$^2\Pi_u$	3.05	0.37
$^4\Delta_g$	3.14	0.73	$^4\Delta_g$	3.13	0.77
$^2\Sigma_u^+$	2.95	0.87	$^2\Sigma_u^+$	2.92	0.85
$^4\Pi_g$	2.85	1.29	$^4\Pi_g$	2.90	1.13

Table 3
The effect of including $4d^{10}$ core in the CASSCF calculations of the electronic states of In_3

State	With $4d^{10}$		Without $4d^{10}$	
	R_e (Å)	θ_e (deg)	R_e (Å)	θ_e (deg)
$^4A_2$	3.01	75.3	2.97	75.2
$^2B_1$	3.36	49.1	3.37	47.6
$^2A_1$	3.62	49.7	3.60	49.6

The energy separations of various electronic states are sensitive to higher-order correlations. In fact, the $^2A_1$ and $^4B_2$ states switch order in comparing CASSCF and MRSDCI calculations. The energy separations of most of the excited states increase at the MRSDCI

level of theory implying stabilization of the lowest electronic states.

The atomization energy, i.e. the energy for the following process

$In_3 \rightarrow 3In$

was calculated by making a long distance calculations ($R=8.0$ Å) for the linear $^4A_2$ state. The MRSDCI calculations yield an atomization energy of 48 kcal/mol for In_3.

Table 4 shows the calculated dipole moments for the electronic states of In_3 at their equilibrium geometries using the MRSDCI natural orbitals. As can be seen from table 4, all the isosceles triangular structures have large dipole moments. The $^4A_2$ and $^2B_2$ states have positive charges at the base atoms while all other isosceles triangular states have positive charges at the apex of the triangle.

Fig. 2 shows the bending potential energy surfaces for the various electronic states of In_3 obtained using the CASSCF method. The $^4A_2$ surface contains a bent minimum which correlated into $^4\Sigma_u^-$ linear state. The $^4B_1$ surface is very narrow near θ_e, goes through a barrier and correlates with the $^4\Delta_g$ linear state. The $^2B_1$ surface also goes through a much smaller barrier. The crossing of $^4A_2$ and $^2B_1$ at $\theta \approx 140°$ is quite interesting. Note that at the CASSCF level of theory $^2\Pi_u$ state with linear geometry is lower. However, the $^4A_2$ (bent), $^4B_1$ (bent), $^2\Pi_u$ (linear), $^2B_1$ (bent) are all nearly degenerate at this level of theory.

3.2. Nature of low-lying electronic states and bonding

Table 5 shows the coefficients of the most important configurations in the CASSCF wavefunctions of the electronic states of In_3. The $1a_1$ orbital is the totally symmetric linear combination of the 5s orbitals on the three atoms. The $2a_1$ orbital is $-In_1(5s)+In_2(5s)+In_3(5s)$ for the $^4A_2$ state where In_1 represents the apex atom of the isosceles triangle. For the $^2A_1$ state, the $2a_1$ orbital is predominantly $In_2(5s)+In_3(5s)$ since the equilibrium geometry of this state is a very acute triangle ($\theta_e \approx 51\%$). The $3a_1$ orbital for the $^4A_2$ state is predominantly made up of the 5s and $5p_y$ and $5p_z$ orbitals of the base atoms. The $1b_2$ orbital for the $^4A_2$ state is predominantly $In_2(5s)-In_3(5s)$ antibonding orbital for both $^4A_2$ and $^2A_1$ states. The $2b_2$ orbital which is occupied for the $^4A_2$ state is predominantly $In(5p_y)-In_2(5p_z)+In_3(5p_z)$ bonding orbital. The $1b_1$ orbital of $^4A_2$ state is $In(5p_x)+In_2(5p_x)+In_3(5p_x)$ bonding orbital in the plane perpendicular to the cluster. This orbital is unoccupied for the $^2A_1$ state (actual density is 0.05). Hence the $^4A_2$ state exhibits slight multiple bonding in the plane perpendicular to the trimer while the $^2A_1$ state is made of in plane bonds. Thus the In–In bond lengths are shorter in the $^4A_2$ state compared to the $^2A_1$ state.

Table 4
Dipole moments of electronic states of In_3 with isosceles triangular geometry

State	μ [a] (D)
$^4A_2$	−0.48
$^4B_1$	0.51
$^2B_1$	0.95
$^2A_1$	0.80
$^2B_2$	−0.65

[a] Positive polarity means the positive charge is on the apex atom of the isosceles triangle.

Table 6 shows the gross, net and overlap Mulliken populations of the electronic states of In_3. As can be seen from table 6, the apex atom has a gross population larger than 3.0 for the $^4A_2$ and $^2B_2$ states while it is smaller than 3.0 for other states. Thus there is charge transfer in these states except the $^4B_2$ state which has an equilateral triangular geometry. In general structures with large angle ($\theta_e > 60°$) equilibrium geometries carry slight negative charges on the central atom while structures with very acute θ_e ($\theta_e < 60°$) carry positive charges on the central atom. This is consistent with the reported dipole moments for these states (table 4). The metal atom s populations are somewhat smaller for all the electronic states. The gross p populations for most of the electronic states are larger than their natural atomic occupations. This seems to suggest some mixing of $5s^25p^1$ and $5s^15p^2$ configurations especially in the $^4A_2$, $^4B_2$, $^2B_2$ and $^4A_1$ states. The d populations are not very large except for the $^4\Sigma_u^-$ linear electronic state of In_3.

Next we discuss differences in bondings and electronic properties of different states for In_3. We use figs. 1 and 2 and tables 5 and 6 as references of our discussion. As seen from fig. 2, the $^4A_2$, $^2B_2$, $^4\Sigma^-$, $^2\Pi_u$ and $^4\Delta_g$ states form linear or relatively large angle

Table 5
CASSCF/CI wavefunctions of electronic states for In_3

State	Coefficient	Configuration									
		$1a_1$	$2a_1$	$3a_1$	$4a_1$	$1b_2$	$2b_2$	$3b_2$	$1b_1$	$2b_1$	$1a_2$
$^4A_2$	0.946	2	2	1	0	2	1	0	1	0	0
	−0.088	2	0	1	2	2	1	0	1	0	0
$^4B_1$	−0.951	2	2	1	1	2	0	0	1	0	0
	−0.084	2	2	1	1	1	0	1	1	0	0
$^2B_1$	0.921	2	2	2	0	2	0	0	1	0	0
	−0.137	2	2	0	0	2	2	0	1	0	0
	−0.121	2	2	2	2	0	0	0	1	0	0
	−0.109	2	2	1	1	1	1	0	1	0	0
	−0.098	2	2	2	1	1	0	0	0	0	1
	−0.090	2	1	1	0	2	0	0	1	2	0
$^4B_2$	−0.962	2	2	1	1	2	1	0	0	0	0
	0.080	2	2	1	1	1	1	1	0	0	0
$^4A_1$	−0.950	2	2	0	0	2	1	0	1	0	1
	0.121	2	2	1	0	2	0	0	1	1	0
	−0.101	2	1	0	0	2	2	0	1	1	0
	0.091	2	1	1	0	2	1	0	1	0	1
	−0.086	2	1	0	1	1	1	1	1	0	1
$^2B_2$	0.938	2	2	2	0	2	1	0	0	0	0
	−0.100	2	2	1	1	2	1	0	0	0	0
	−0.096	2	0	2	0	2	1	0	1	1	0
$^2A_1$	−0.943	2	2	2	1	2	0	0	0	0	0
	0.143	2	2	0	1	2	2	0	0	0	0
	0.117	2	2	2	1	1	1	0	0	0	0
	0.100	2	2	0	1	2	0	0	0	2	0
		$1\sigma_g$	$2\sigma_g$	π_u	$3\sigma_g$	$1\sigma_u$	$2\sigma_u$	$3\sigma_u$	π_g		
$^4\Sigma_u^-$	0.942	2	2	2	0	2	1	0	0		
	0.115	2	1	1	0	2	2	0	1		
	−0.091	2	1	1	0	2	2	1	0		

minima compared to $^2A_1$, $^2B_1$, $^4B_1$, and $^4B_2$ states which form very acute triangle or equilateral triangular minima. These differences in the geometries and the nature of potential energy surfaces may be puzzling. Thus it was decided to analyze these further using overlap populations, electronic configurations, etc.

In general, electronic states which exhibit multiple bonding of the central atom to side atoms tend to form linear structures or large angle structures. The In–In overlap populations of the central atom with corner atoms, as well as the In–In base atoms' overlap for different states seem to provide significant insights and clues to the nature of potential energy surfaces and why some states form very acute angle minima whereas other electronic states form large angle or linear minima.

As seen from table 6, the In–In overlaps of the central–corner atoms are considerably larger for the $^4A_2$ and $^4\Sigma_u^-$ states compared to other doublet and quar-

Table 6
Mulliken population analyses for electronic states of In_3

State	Net							Gross							Overlap [a]
	M_1 [b]	M_2 [c]	M_1(s)	M_2(s)	M_1(p)	M_2(p)	M_1(d)	M_2(d)	M_1 [b]	M_2 [c]	M_1(s)	M_2(s)	M_1(p)	M_2(p)	M_1(d)	M_2(d)	
$^4A_2$	2.762	5.552	1.677	3.414	0.921	1.756	0.041	0.082	3.105	5.896	1.728	3.616	1.326	2.192	0.052	0.086	0.686
$^4B_1$	2.698	5.900	1.703	3.328	0.771	2.234	0.042	0.094	2.899	6.100	1.821	3.524	1.034	2.484	0.044	0.094	0.402
$^2B_1$	2.750	5.940	1.949	3.058	0.695	2.172	0.044	0.092	2.906	6.094	1.860	3.478	0.995	2.526	0.051	0.090	0.310
$^4B_2$	2.846	5.844	1.786	3.510	0.893	2.008	0.037	0.078	3.001	5.998	1.839	3.686	1.122	2.238	0.040	0.076	0.312
$^2A_1$	2.808	5.98	1.860	3.620	0.787	2.196	0.040	0.090	2.914	6.086	1.877	3.654	0.997	2.344	0.040	0.086	0.212
$^2B_2$	2.859	5.744	1.828	3.824	0.907	1.862	0.047	0.086	3.058	5.942	1.786	3.704	1.217	2.146	0.054	0.092	0.398
$^4A_1$	2.700	5.826	1.586	3.584	0.843	1.906	0.037	0.060	2.937	6.064	1.770	3.688	1.125	2.310	0.041	0.066	0.474
$^4\Sigma_u^-$	2.813	5.228	1.412	3.516	1.189	1.328	0.036	0.059	3.293	5.707	1.498	3.448	1.638	1.973	0.156	0.286	0.959

[a] Overlap between the apex atom and the two base atoms.
[b] Apex atom. [c] The two base atoms.

tet states which form small angle minima. In the case of $^4\Sigma_u^-$ state linear state, In–In central–corner overlaps are the largest (0.96) since direct overlap of the central atom to the other two atoms is most favored in this orientation. The electronic configuration of the linear $^4\Sigma_u^-$ state is $1\sigma_g^2 2\sigma_g^2 1\sigma_u^2 2\sigma_u 1\pi_u^2$. Evidently, the occupancy of the π_u orbital suggests multiple corner bonds in the linear state (see fig. 1). Thus the $^4\Sigma_u^-$ state exhibits shorter In–In bond lengths of 2.90 Å.

As the molecule is bent from its linear $^4\Sigma_u^-$ state, the overlaps of the base atoms increase leading to a structure in which both the side and base overlaps attain optimal values for that state. Consequently, the bent $^4A_2$ state geometry in fig. 1 ($\theta_e \approx 71°$) is most consistent with this qualitative description. The In–In overlap at the base is small (R(base) = 3.43 Å) but compensates for the partially destroyed multiple bonding overlap along the central–corner atoms of the linear structure. The final MRSDCI $^4A_2$–$^4\Sigma_u^-$ separation is only 0.07 eV, confirming this qualitative description.

The $^2B_2$ state correlates into the $^2\Sigma_u^+$ linear state. The $^2\Sigma_u^+$ nature of this state suggests occupation of a $2\sigma_u$ antibonding orbital ($2b_2$ in table 5). The antibonding interaction is the largest for the linear structure. Thus bending the molecule is favorable since it reduces the antibonding interaction thereby leading to a bent geometry (see fig. 2). At the bent $^2B_2$ minimum, the repulsive interaction in the $2\sigma_u(2b_2)$ orbital is minimized.

The $^2A_1$ and $^2B_2$ states could be envisaged as the Jahn–Teller components of a $^2E'$ equilateral triangular structure. Consequently, the Jahn–Teller distortion splits the $^2E'$ state into the $^2A_1$ component with $\theta_e < 60°$ ($\theta_e = 51°$) and the $^2B_2$ component with $\theta_e > 60°$ (74.4°). These two structures are analogues of the two nearly degenerate, $^2A_1$ and $^2B_2$ Jahn–Teller components of Au_3 and Ag_3 clusters discussed in previous studies from our laboratory [31,32]. The MRSDCI splitting of $^2B_2$ and $^2A_1$ states is only 0.1 eV confirming the Jahn–Teller picture of these two states. If these two states are true Jahn–Teller components, then they must cross at $\theta = 60°$. As seen from fig. 2, the $^2A_1$ and $^2B_2$ curves cross very close to $\theta = 60°$. A small difference is due to the size inconsistency in the treatment of electron correlations in these two states. Furthermore, since $^2B_2$ and $^2A_1$ states are Jahn–Teller components of $^2E'$, the central In atom in the two

states carries opposite charges. In the case of $^2A_1$ the central atom carries approximately 0.086 charge as derived from gross Mulliken population in table 3. For the $^2B_2$ state the central atom carries -0.058 charge. Note that the dipole moments of $^2A_1$ and $^2B_2$ states are 0.80 and -0.65 D, respectively (table 4). Thus the dipole moments of these two states follow an approximate "center of gravity" rule in that the $^2A_1$ state differs more from the ideal equilateral triangular geometry. The ideal $^2E'$ structure would have zero dipole moment. This structure is a cusp in the global potential energy surface.

The $^4B_1$ and $^2B_1$ states exhibit similarities in their equilibrium geometries as seen from fig. 1. In both these states, there is considerable In–In overlap at the base atoms of the isosceles triangle, thereby bringing the base atoms much closer. This is offset by the smaller In–In overlaps at the side of the isosceles triangle. As seen from table 6, in $^4B_1$, $^2B_1$ and $^2A_1$ states, the total populations of the two M_2 atoms (base) are considerably larger than the central atom. There is clearly multiple bonding along the base atoms in the $^4B_1$ and $^2B_1$ states.

The above discussions evidently reveal that the differences in equilibrium geometries and potential energy surfaces are governed by orbital interactions, metal–metal overlaps, charge transfers and multiple bondings along the base or the sides. If multiple bonding or strong orbital overlap occurs at the base, then the structure tends to be very acute. If multiple bonding occurs at the central–corner atoms, the structure exhibits large angle minima or is linear. The $^2B_2$ and $^2A_1$ states are Jahn–Teller components of the $^2E'$ state. In the $^4B_2$ state there is a perfect balance of base and side overlaps leading to an equilateral triangular structure.

The spin–orbit effects on the electronic states of In_3 could be important since the atomic $^2P_{3/2}$–$^2P_{1/2}$ splitting of the indium atom is 2200 cm^{-1} [33]. As noted in section 2 the spin–orbit effects were incorporated using the relativistic CI (RCI) method. First, the effect of the spin–orbit term on the geometry was investigated for two low-lying electronic states. It was found that the R_e and θ_e values did not change at all ($\Delta\theta_e = 0°$, $\Delta R_e = 0.00$ Å) by the spin–orbit term. The spin–orbit term made more appreciable contribution to the energy separations. Thus RCI calculations for all the states were carried out at the MRSDCI optimized geometries.

Table 7 shows the effect of spin–orbit coupling on the electronic states of In_3. The electronic states are lowered in energy overall by the spin–orbit coupling. However, the splitting between different spin–orbit states for a given electronic state is somewhat small. The spin–orbit stabilization is about 0.01 eV for most of the electronic states. Thus, spin–orbit effects are not very significant for the electronic states of In_3.

3.3. Comparison of electronic states of In_3 with Ga_3 and predictions on Tl_3

In this section, we compare the electronic states of In_3 with its lighter analogue, namely, Ga_3. In an earlier investigation, the present authors [12] studied the electronic states of Ga_3. The two trimers differ in many ways. For Ga_3, the $^2A_1$ state is the ground state while the $^4A_2$ state is about 0.24 eV above the ground state. For In_3, however, the $^4A_2$ and $^4B_1$ states are considerably lower in comparison to the $^2A_1$ state. The $^2A_1$ state, in fact, is 0.35 eV above the $^4A_2$ state. For both the species, $^4A_1$ state of linear geometry is the highest in energy. For Ga_3, the $^4A_1$ state is 1.38 eV above the ground state while the corresponding state

Table 7
The effect of the spin–orbit coupling term on the electronic states of In_3

State	E (eV)
$^4A_2(\alpha\alpha\alpha)$	0.000
$^4A_2(\alpha\alpha\beta+\alpha\beta\alpha+\beta\alpha\alpha)$	0.006
$^4B_1(\alpha\alpha\alpha)$	0.011
$^4A_2$	0.015
$^4B_1(\alpha\alpha\beta+\alpha\beta\alpha+\beta\alpha\alpha)$	0.015
$^4B_1$	0.025
$^2B_1(\alpha)$	0.121
$^2B_1$	0.125
$^4B_2(\alpha\alpha\beta+\alpha\beta\alpha+\beta\alpha\alpha)$	0.360
$^4B_2(\alpha\alpha\alpha)$	0.361
$^4B_2$	0.365
$^2A_1(\alpha)$	0.452
$^2B_2(\alpha)$	0.456
$^2A_1$	0.465
$^2B_2$	0.465
$^4A_1(\alpha\alpha\alpha)$	0.779
$^4A_1(\alpha\alpha\beta+\alpha\beta\alpha+\beta\alpha\alpha)$	0.783
$^4A_1$	0.785

for In_3 is only 0.77 eV above the ground state. In general, the seven electronic states are more closely packed for In_3 in comparison to Ga_3. The metal–metal bond lengths are longer for In_3 as expected in comparison to Ga_3. The difference in the properties of Ga_3 and In_3 noted above seems to arise from both relativistic effects and the fact that the atomic energy separations are lower for In in comparison to Ga. For example, the ^4P state arising from $4s4p^2$ is 38000 cm^{-1} above for Ga while the corresponding state ($5s5p^2$) is 35000 cm^{-1} above the ground state for In [33].

The dramatic difference between the electronic states of Ga_3 and In_3 is in the ionity of the metal–metal bonding. The dipole moments of the electronic states of In_3 are considerably larger in comparison to the corresponding states of Ga_3. This trend is expected since the indium atom is more metallic (more electropositive) than gallium atom.

In comparing the Mulliken populations of the electronic states of Ga_3 and In_3, we note that the metal–metal overlaps are much smaller for In_3. This is mainly because the bonding is weaker in In_3 in comparison to Ga_3. For example, the $M–M_2$ overlaps for $^4A_2$ of Ga_3 and In_3 are 0.931 and 0.686, respectively. The metal s populations are considerably smaller for Ga_3 in comparison to In_3. This should be mainly due to relativistic mass–velocity stabilization of the $5s^2$ shell of the indium atom in comparison to the $4s^2$ shell of the gallium atom. This is the primary factor for the weakening of the metal–metal bond in the electronic states of In_3 in comparison to the electronic states of Ga_3. The metal d populations are considerably larger for Ga_3 in comparison to In_3. The gross d populations of the electronic states of Ga_3 are between 0.14 and 0.27 while the corresponding populations for In_3 are 0.07–0.09. Thus, the metal d orbital participation is somewhat smaller for In_3.

Based on the above comparison of Ga_3 and In_3, some predictions can be made on the properties of low-lying electronic states of Tl_3. In our laboratory, we completed extensive calculations on the potential energy curves of Ga_2 [34] and In_2 [24], whereas Christiansen and Pitzer [35] completed calculations on the potential energy curves of low-lying states of Tl_2. The ground state of Tl_2 was found to be a 0_u^- state arising from a $^3\Pi_u$ state with very small binding energy. The R_e of In_2 was found to be 3.14 Å, whereas the R_e of 0_u^- state of Tl_2 is 3.54 Å. The much longer bond length and weaker Tl–Tl bond in Tl_2 is mainly due to the inert pair effect which is actually a consequence of the relativistic mass–velocity stabilization of the $6s^2$ shell of Tl. Hence for Tl_3, the inert-pair effect and relativistic spin–orbit effects will play a major role in the determination of electronic properties. Based on the theoretical bond lengths for Tl_2 and Ga_2, we believe that Tl–Tl bond lengths should be about 0.4 Å longer. For example, the $^2B_2$ and $^2A_1$ Jahn–Teller components of Tl_3 should still have $\theta_e > 60°$ and $\theta_e < 60°$, respectively. But Tl–Tl bond length in the $^2A_1$ state for the side atoms would be roughly 3.9 Å, while the base bond length would be 3.4 Å, if θ_e were to be about the same. Similarly, in the $^2B_2$ state Tl–Tl side bond lengths would be 3.5 Å while the base bond length would be 4.1 Å. Those states in which $5s^25p^1–5s5p^2$ mixings were found for In_3 would become less favorable for Tl_3 due to the operation of the inert pair effect. These predictions are only speculations which are yet to be verified by relativistic calculations of comparable quality.

4. Conclusion

In this investigation, we carried out CASSCF/MRSDCI calculations on seven low-lying electronic states ($^4A_2$, $^4B_1$, $^2B_1$, $^4B_2$, $^2A_1$, $^2B_1$ and $^4A_1$) and their potential energy surfaces for In_3. The MRSDCI calculations included up to 177000 configurations. Two nearly degenerate states of $^4A_2$ and $^4B_1$ symmetries with isosceles triangular geometries were found as candidates for the ground state ($^4A_2$: R_e(side) = 2.95 Å, R_e(base) = 3.43 Å; $^4B_1$: R_e(side) = 3.12 Å, r_e(base) = 2.89 Å). The atomization energy of In_3 was calculated as 48 kcal/mol at the MRSDCI level of theory. The analyses of bondings, Mulliken populations and dipole moments revealed that orbital overlaps, charge transfers and the leading configurations determine the nature of metal–metal bonds in the low-lying states of In_3. The $^2B_2$ and $^2A_1$ states of In_3 were interpreted as Jahn–Teller components of a $^2E'$ state. Electronic states with $\theta_e > 60°$ were found to carry negative charges on the central atom (positive charges on the side atoms) while states with $\theta_e < 60°$ were found to carry positive charges on the central atom.

The analyses of Mulliken populations revealed $5s^25p^1-5s^15p^2$ mixing in some of the electronic states. The properties and equilibrium geometries of In_3 were compared with Ga_3.

Acknowledgement

This research was supported by US National Science Foundation through grant No. CHE8818869. PYF thanks Shanghai Metallurgy Institute, Academia Sinica for providing a leave of absence.

References

[1] R.C. Baetzold and J.H. Hamilton, Progr. Solid State Chem. 15 (1983) 1.
[2] M.D. Morse, Chem. Rev. 86 (1986) 1049.
[3] M.E. Geusic, M.D. Morse and R.E. Smalley, J. Chem. Phys. 82 (1985) 590.
[4] M.D. Morse, M.E. Geusic, J.R. Heath and R.C. Smalley, J. Chem. Phys. 82 (1985) 2293.
[5] S.C. O'Brien, Y. Liu, Q. Zhang, J.R. Heath, F.K. Tettel, R.F. Curl and R.E. Smalley, J. Chem. Phys. 84 (1986) 1074.
[6] R.S. Grev and H.F. Schaefer III, Chem. Phys. Letters 119 (1985) 111.
[7] G.H.F. Diercksen, N.E. Gruner, J. Oddershede and J.R. Sabin, Chem. Phys. Letters 117 (1985) 29.
[8] K. Balasubramanian, Chem. Phys. Letters 135 (1987) 283.
[9] K. Balasubramanian, Chem. Phys. Letters 125 (1986) 400.
[10] K. Balasubramanian, J. Chem. Phys. 85 (1986) 3401.
[11] K. Balasubramanian, J. Chem. Phys. 87 (1987) 3518.
[12] K. Balasubramanian and P.Y. Feng, Chem. Phys. Letters 146 (1988) 155.
[13] K. Raghavachari, J. Chem. Phys. 83 (1985) 3525.
[14] K. Raghavachari, J. Chem. Phys. 84 (1986) 5622.
[15] H. Basch, Chem. Phys. Letters 136 (1987) 298.
[16] J.A. Howard, R. Sutcliffe, T.S. Tse, H. Dahamane and B. Mile, J. Phys. Chem. 89 (1985) 3595.
[17] V.E. Bondybey, W.D. Reents Jr. and M.L. Mandich, unpublished results.
[18] R.G. Wheeler, K. Lai Hing, W.L. Wilson and M.A. Duncan, J. Chem. Phys. 88 (1988) 2831.
[19] K. Lai Hing, R.G. Wheeler, W. Wilson and M.A. Duncan, J. Chem. Phys. 87 (1987) 3401.
[20] K. Lai Hing, P.Y. Cheng and M.A. Duncan, J. Chem. Phys. 88 (1988) 2831.
[21] M.E. Geusic, R.R. Freeman and M.A. Duncan, J. Chem. Phys. 88 (1988) 163.
[22] K.M. Ervin, J. Ho and W.C. Lineberger, J. Chem. Phys. 88 (1988) 4514.
[23] S. Taylor, G.W. Lemire, Y.M. Hamrick, Z. Fu and M.D. Morse, J. Chem. Phys. 88 (1988) 5517.
[24] K. Balasubramanian and J.Q. Li, J. Chem. Phys. 88 (1988) 4979.
[25] Z. Fu, G.W. Lemire, Y.M. Hamrick, S. Taylor, J.C. Shui and M.D. Morse, J. Chem. Phys. 88 (1988) 3524.
[26] M.H. McAdon and W.A. Goddard III, J. Phys. Chem. 87 (1987) 2607.
[27] L.A. LaJohn, L.F. Pacios, P.A. Christiansen, R.B. Ross, T. Atashroo and W.C. Ermler, J. Chem. Phys. 97 (1987) 2812.
[28] K. Balasubramanian, J. Chem. Phys. 89 (1988) 5731.
[29] K. Balasubramanian, Chem. Phys. Letters 127 (1986) 585.
[30] R.M. Pitzer and N.W. Winter, J. Phys. Chem. 92 (1988) 3061.
[31] K. Balasubramanian and M.Z. Liao, Chem. Phys. 127 (1988) 313.
[32] K. Balasubramanian and M.Z. Liao, J. Chem. Phys. 86 (1987) 3587.
[33] C.E. Moore, Tables of Atomic Energy Levels, Vol. 3 (Natl. Bur. Std., Washington, 1971).
[34] K. Balasubramanian, J. Phys. Chem. 90 (1986) 6786.
[35] P.A. Christiansen and K.S. Pitzer, J. Chem. Phys. 74 (1981) 1162.